Unique topological surface states of full-Heusler topological crystalline insulators

Anh Pham and Sean Li

School of Materials Science and Engineering, The University of New South Wales, Sydney, New South Wales, Australia 2052

(Received 30 October 2016; published 13 March 2017)

Our theoretical analysis reveals that a family of full-Heusler materials exhibit unique topological surface states with type-I and type-II Dirac quasiparticles. The type-I Dirac surface state is characterized by an enclosed Fermi surface, while the type-II Dirac surfaces occur at the touching of the electron and hole pockets. In addition, due to the layered nature of the full-Heusler crystals structured with a wide range of various elements, such structures induce multiple Dirac surface states with different Lifshitz transitions protected by more than one mirror plane.

DOI: 10.1103/PhysRevB.95.115124

I. INTRODUCTION

Topological crystalline insulator (TCI) is new class of topological insulator in which the topology of the band structure is protected by the mirror symmetry rather than the time reversal symmetry [1,2]. As a result, the surface Dirac cone of a TCI is not required to be located at a time reversal invariant momentum, and it can glide along the two-dimensional (2D) Brillouin zone perpendicular to the mirror plane [3–10]. This property allows the Dirac dispersion of TCI to violate other symmetries, such as the Lorentz symmetry, which can lead to new surface quasiparticles, such as the type-II Dirac fermions. Analogous to type-II Weyl dispersions [11–14] in the bulk, type-II Dirac cones can occur on certain crystal momentum on the surface of a TCI. As a result, the Fermi surfaces of the type-II Dirac fermions are formed at the touching of open electron and hole pockets rather than exhibiting an enclosed circular behavior.

Heusler materials have attracted recent interest as a new class of multifunctional topological materials [15–18]. Studies on these materials primarily have focused on half-Heusler structures as strong topological insulators induced by their inverted band structure at an odd time reversal momentum such as Γ [19]. However, the investigation on full-Heusler (FH) materials is very limited because their band structures tend to be half metallic [20]. In FH materials, the structure is composed of a layer of simple cubic X_2 sublattice in between the Y-Z rock salt layers. In principle, an appropriate selection of the chemical elements in the Y-Z layer can result in a narrow gap semiconductor. Moreover, the elements in this rock salt layer are arranged in a face-centered-cubic (fcc) lattice, which contains a mirror invariant plane (110), making them a potential candidate for the topological crystalline insulating class due to the similarity with IV–VI TCI materials, such as SnTe.

In this paper, we demonstrate the existence of a new class of TCI in a family of full-Heusler thermoelectric materials with ten valence electrons [21], which exhibits type-I and type-II Dirac surfaces. Due to the intrinsic band inversion originated from the Y and Z sites, these materials can be characterized as a TCI due to the existence of a (110) mirror plane. However, different from the well-known IV–VI TCI, the nature of layered structure makes these FH materials exhibit rich topological surface states, thus hosting the multiple protected Dirac nodes with type-I and type-II characteristic on the same crystal structure due to the protection of the different mirror planes.

To understand the different topological behaviors of the FH structure, we investigated (i) the effective surface Hamiltonian of the fcc lattice in SnTe to understand the microscopic origin of the type-II Dirac surface, (ii) the bulk band structures of the FH materials, and (iii) the surface energy spectrum of the representative material candidates with examples of Ca_2AuBi, Li_2BiTl, and Ca_2HgPb to show the different type-I and type-II Dirac surfaces in this class of TCI.

II. EFFECTIVE MODEL HAMILTONIAN OF TYPE-II DIRAC SURFACE

To identify the different topological surface states of the FH structure, we revisit the model of the surface Hamiltonian with fcc lattice as represented by the SnTe-type TCIs. These materials possess two types of topological surfaces, depending on the projection of the bulk L symmetry points on the 2D surface Brillouin zone [4–6]. In particular, the two L points are projected to the same point $\overline{X_1}(\overline{X_2})$ in the [001]-orientation, resulting in two Dirac cones at the non-TRIM points along the $\overline{\Gamma X_1}$ direction or on the $\overline{\Gamma X}$ line in the [110] surface. As a result, the Fermi surfaces exhibit a Lifshitz transition between the Dirac points on the [001]/[110] surfaces. For the [111] direction, one L point is projected to $\bar{\Gamma}$, while the other three L points are projected to the $\overline{M}$, producing two linear band crossings at the time reversal symmetric momenta.

Using symmetry principles, the four-band model of the [001] surface with type-I Dirac cones can be described by an effective $\mathbf{k}\cdot\mathbf{p}$ Hamiltonian [4]

$$H_{X_1} = (v_1 k_1 s_2 - v_2 k_2 s_1) \otimes I + m s_o \otimes \tau_1 + \delta s_1 \otimes \tau_2, \quad (1)$$

where v_1 and v_2 are the Fermi velocities in the k_1 and k_2 axes; s_i and τ_i are the Pauli matrices in the spin and orbital basis; $\otimes$ is the Kronecker product. This Hamiltonian preserves two mirror symmetries of $M_1(-is_1 \otimes \tau_o)$ and $M_2(-is_2 \otimes \tau_1)$, which are the C_2 rotational symmetry $(-is_1 \otimes \tau_3)$ and the time reversal symmetry $T(is_2 \otimes \tau_o K)$. To induce a type-II Dirac surface in the k_2 axis in Eq. (1), we consider different perturbations with up to a first of order k_2. Possible additional terms preserving the aforementioned symmetries are $(s_o \otimes \tau_2)k_2$ and $(s_1 \otimes \tau_2)k_2$. These terms break the particle-hole symmetry, thus creating two titled Dirac cones characterizing the type-II Dirac dispersions. Additionally, since the Dirac cone in Eq. (1) is maintained as long as the M_1 symmetry is preserved, another symmetry term such as $(s_o \otimes \tau_o)k_2$ can potentially exist in Eq. (1), which also induces a type-II

Dirac cone. Such a term would break M_2, C_2, and T; thus, it can have an interesting effect with respect to the in-plane magnetotransport. Consequently, in essence the type-II Dirac surface can arise if there is a strong particle-hole symmetry breaking or time reversal symmetry breaking on the surface orientation such as [001] and [110].

III. COMPUTATIONAL METHODS

The bulk geometry and band structure were studied using the density functional theory (DFT) code Vienna *Ab initio* Simulation Package (VASP) within the projector-augmented wave (PAW) method [22,23] with a dense k mesh of $15 \times 15 \times 15$ via the Monkhorst-Pack scheme [24]. The bulk geometry and electronic band structure were also investigated with the Perdew-Burke-Ernzerhof (PBE) exchange functional [25]. The band inversion was further checked using the Heyd-Scuseria-Ernzerhof hybrid functional (HSE06) functional [26,27], with the spin-orbit effect due to tendency of the PBE method to underestimate the band gap [28]. To characterize the surface energy spectrum and the Fermi surface, a maximally localized Wannier function (MWLF) [29,30] based tight binding method was employed to calculate the surface Green function via an iterative scheme [31,32]. To verify the stability of the FH structures, the phonon spectrum was studied using the Phonopy code [33]. The phonon spectrum, the surface spectrum and the bulk band structures of other FH materials are presented in the Supplemental Material [34].

IV. BULK BAND STRUCTURE OF FH MATERIALS

Crystallographically, the FH materials are crystallized in a simple fcc structure with the $Fm3m$ (No. 225) space group containing two different sublattices of X and Y-Z, as shown in Fig. 1(a). The sublattice X hosts group-I and group-II elements, such as Li, Ca, Sr, and Ba, acting as positively charged reservoirs to balance the negatively charged Y-Z layers. In the Y-Z layer, the rock salt sublattice is composed of elements with large spin-orbit effect. The similarity of the crystal structure of X_2YZ to SnTe makes these materials an

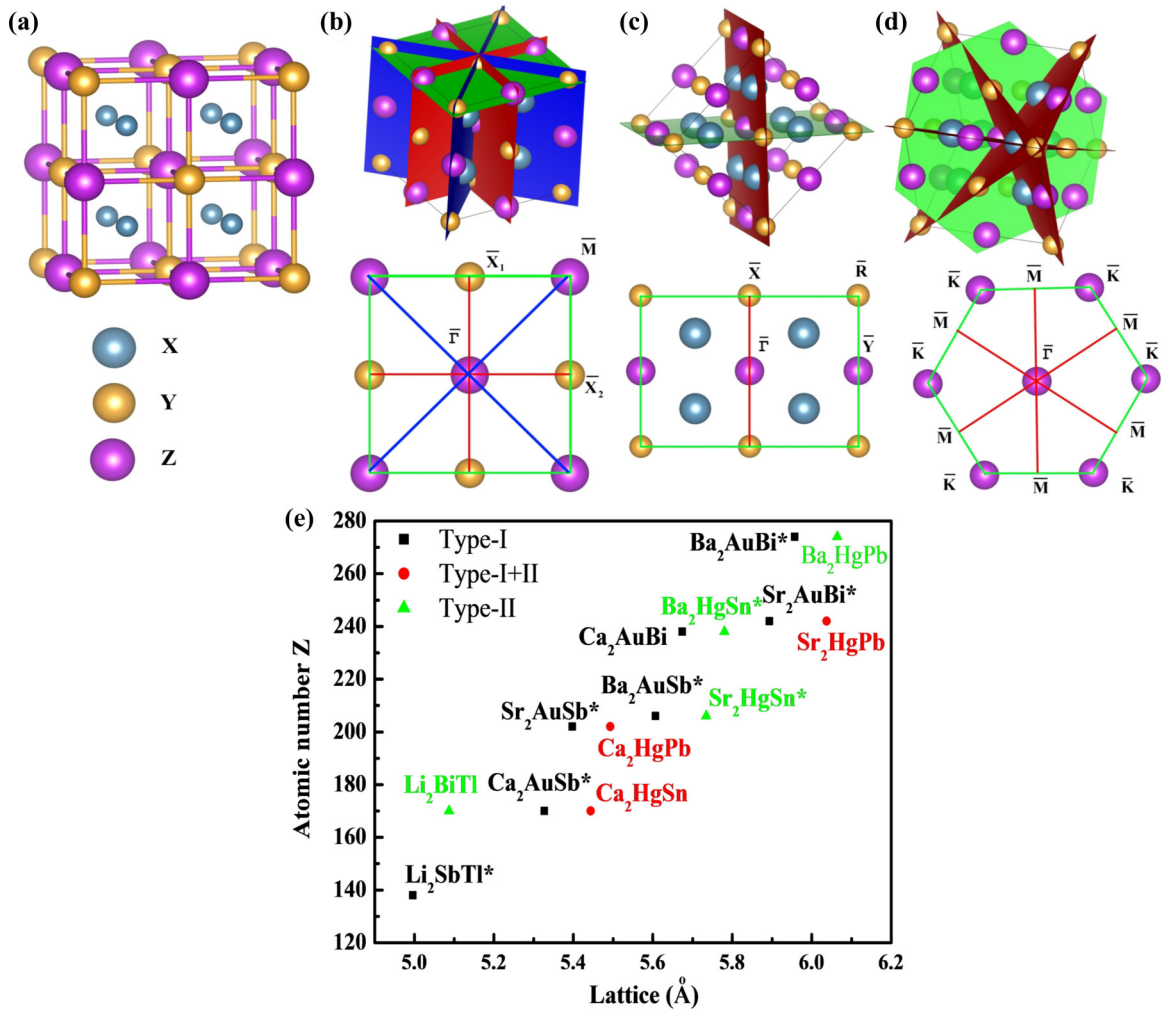

FIG. 1. Crystal structures of FH X_2YZ. (a) Bulk crystallography; (b) [001]-plane (top) and the 2D Brillouin zone (bottom); (c) [110]-plane (top) and the 2D Brillouin zone (bottom); (d) [111]-plane (top) and the 2D Brillouin zone (bottom). The (110) mirror plane is highlighted in red, the (001) plane is highlighted in blue and the crystal plane is highlighted in green for the three-dimensional (3D) and 2D views. (e) The summary of the potential materials containing type-I, type-II Dirac fermions, or both on the [001] surface. Materials with * are normal semiconductors but can be tuned to TCI through either compressive or tensile strain.

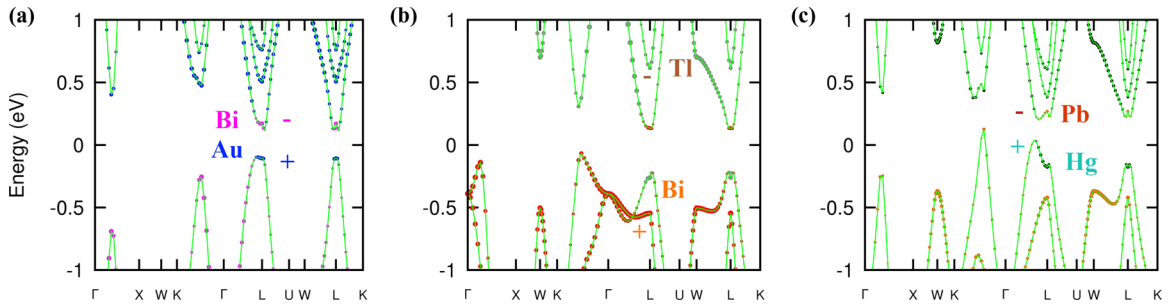

FIG. 2. Bulk band structures with p orbitals of the elements in the rock salt layer. (a) Ca_2AuBi; (b) Li_2BiTl; (c) Ca_2HgPb. The spin-orbit effect was included in all the calculations. The even parity is (+), and odd parity is (−).

ideal candidate for TCI if a band inversion exists at an even numbers of the time reversal symmetry momenta (TRIM).

In the X_2YZ structure, the bulk band structures of Ca_2AuBi, Li_2BiTl, and Ca_2HgPb undergo a parity exchange with the spin-orbit effect, resulting in a parity exchange with an even parity (+) at the top valence band and an odd parity (−) in the conduction band at L (0.5, 0.5, 0.5), as evident in the hybrid functional calculation, shown in Fig. 2. Because there are four L points in the first Brillouin zone, X_2YZ is topologically trivial in the Z_2 class due to an even number of L points (see Supplemental Material [34]), but owing to the existence of the mirror plane (110) and on different crystal orientations [Figs. 1(b)–1(d)], the topology of these FH materials can be described as TCI. To further verify the nontrivial topology, we studied the momentum resolved surface spectrum and the Fermi surfaces on different surface orientations.

Based on these results, the different types of topological surface states are classified as in Fig. 1(e). Overall, material, such as Ca_2AuBi, is considered to be intrinsic type-I TCI, and the transition between the normal semiconductor to TCI can be tuned by controlling external strain through manipulating the elements that have different atomic sizes for $X =$ Ca, Sr, Ba $Y =$ Au, and $Z =$ As, Sb, Bi due to the similarity of their bulk band structures with Ca_2AuBi. These materials have a direct bulk band structure similar to SnTe; thus, their [001] and [110] orientations can only host the type-I Dirac dispersion. For $X =$ Li and $Z =$ Tl, the different characteristic of the topological surface states are related to the Y element (Sb or Bi), which can create a particle-hole symmetry breaking in the bulk band structure, which can result in either type-I or type-II Dirac surface only. On the other hand, in FH materials with $Y =$ Hg and $Z =$ Sn and Pb, these materials can host both type-I and type-II Dirac surfaces on the same [001] orientation due to asymmetry band inversion at the bulk L point and the protections of the two mirror planes (110) and (001). In addition, the existence of multiple Dirac surfaces in material such as Ca_2HgPb and Sr_2HgPb is also due to the different orbital arrangements in the Y-Z layer at the low energy level in comparison to material such as Ca_2AuBi (see Supplemental Material [34]). Specifically, Ca_2AuBi contains Au's p_x and Bi's p_x and p_y dominating the valence and conduction bands, respectively. Such an orbital distribution resembles SnTe, which contains only a type-I Dirac surface. On the other hand, in the bulk band structure of Ca_2HgPb, Hg's p_x and p_y orbitals dominate the valence band, while Pb's p_x, p_y, and p_z orbitals dominate the conduction band. To demonstrate these vastly different topological surfaces, the surface energy spectra were investigated for Ca_2AuBi, Ca_2HgPb, and Li_2BiTl, as the materials representative of the different roles of material chemistry and the mirror planes in TCI.

V. DIRAC SURFACES

A. Type-I Dirac fermions in Ca_2AuBi

As observed in Fig. 3(a), the energy spectrum of the [001] surface shows a single band crossing in the $\overline{\Gamma X}$ direction as two L points are now projected to the same $\overline{X_1}(0.5,0)$ TRIM point. Consequently, the pair of Dirac cones is topologically protected by a mirror Chern number (MCN) $|N_m| = 2$, since the mirror plane (110) lies on the $\overline{\Gamma X_1}$ direction. For the [110] orientation [Fig. 3(b)], two L points are projected to $\overline{X}(0.5,0)$, and the other two L points are projected to $\overline{R}(0.5,0.5)$. Because $\overline{X}(0.5,0)$ on the [110] orientation has the same mirror symmetry as $\overline{X_1}(0.5,0)$ on the (001) surface, only a single Dirac point can be observed along the $\overline{\Gamma X_1}$ direction. However, along the $\overline{R}(0.5,0.5) - \overline{\Gamma}(0.0,0.0)$ direction, the surface state exhibits an energy gap due to the interaction between the other two L valleys. For the (111) surface, the Au and Bi terminations play different roles to determine the band structure of this system [Fig. 3(c)]. Two Dirac cones are observed on (111) surface at the two TRIM points $\bar{\Gamma}$ and $\overline{M}$. For the Bi termination, the Dirac points occur close to the bottom of the conduction band and just below the top valence band for the Au termination. These Dirac points on are also topologically protected since they belong to the three (110) mirror planes on the 2D Brillouin zone.

As the Fermi energy varies, the Dirac surfaces on the (001) and (110) surfaces undergo a Lifshitz transition. To demonstrate this behavior, we studied the Fermi surfaces on the [110] termination from −0.058 to 0.02 eV [Fig. 3(d)]. As the Fermi energy increases from the valence band to the conduction band, the energy contour exhibits a Lifshitz transition. For the Fermi level below −0.058 eV, the energy surface contains a small electron pocket and a large hole pocket with a circular shape centered at the $\overline{X}(0.5,0)$ point. As the energy level increases, the energy contour changes its topology. The hole pocket is shrunk, and the electron pocket is enlarged, further moving away from the $\overline{X}(0.5,0)$ point. This results in two disconnected elliptical shapes. This transition from a connected elliptical structure to two disconnected shapes is characteristic of the Lifshitz transition. As the Fermi level increases closer to the Dirac points, the size of the

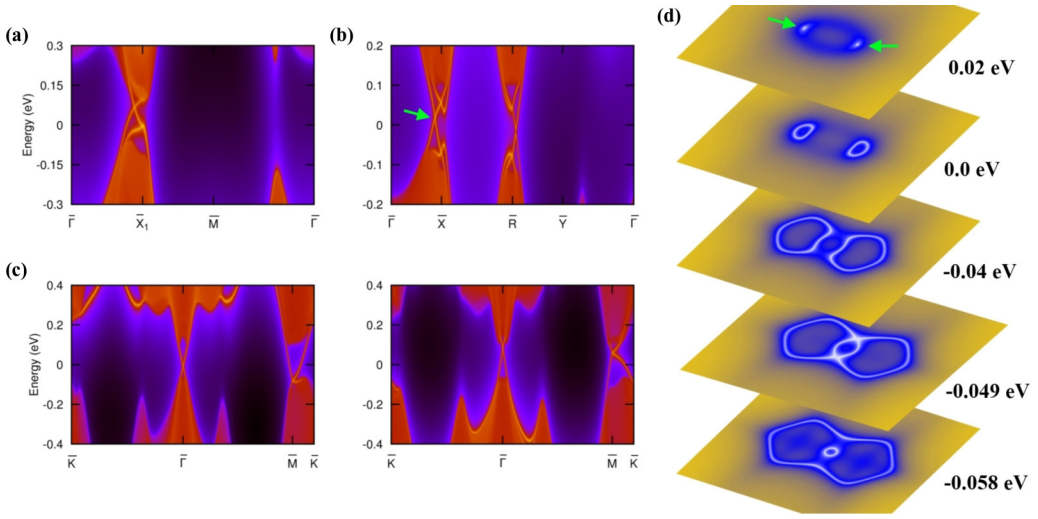

FIG. 3. Surface energy spectrum and Fermi surfaces of type-I TCI Ca_2AuBi. (a) [001] orientation with Au-Bi termination; (b) [110] orientation; (c) [111] orientation with Au (left) and Bi (right) termination. (d) Constant energy contours of the [110] orientation at different levels. The green arrow shows the type-I Dirac node. The energy spectra were obtained from 50 slabs.

crescent shaped Fermi surfaces are shrunk further to the two Dirac points located symmetrically away from the $\overline{X}(0.5,0)$. A similar transition also happens as the energy level is lowered from the bulk conduction band to the Dirac points.

B. Type-II Dirac fermions in Li_2BiTl

In Li_2BiTl, a new type of Dirac surfaces appear along the [001] and [110] orientation. As shown in Fig. 4(a), on the (001) surface with Tl-Bi termination, the bulk valence and conduction bands become indirect, but they are still connected to each other via a helical surface states. However, different from the Dirac states observed on the same orientation and termination of Ca_2AuBi, one of the Li_2BiTl surface chiral states bends over to connect the bulk bands inside the energy gap and intersects the other surface modes at a single point in the $\overline{\Gamma X_1}$ direction. As a result, a pair of Dirac cones still occurs away from the $\overline{X_1}(0.5,0)$ point, but they are now tilted, showing the typical characteristics of a type-II Dirac surface. Similarly, the type-II Dirac surface modes also occur on the $\overline{\Gamma X}$ direction due to the existence of (110) mirror plane along the $\overline{\Gamma X}$ line [Fig. 4(b)]. Based on the numbers of the Dirac modes, a MCN of $|N_m| = 2$ is inferred.

Interestingly, on the (111) surface, the Tl and Bi terminations only exhibit the type-I Dirac surface at the two TRIM $\bar{\Gamma}$ and $\overline{M}$ points. The absence of the type-II Dirac surface can be understood based on the symmetry argument. In addition to the mirror plane (110), there is also a threefold rotation axis C_3 and time reversal-symmetry that forbids any off diagonal term in the surface Hamiltonian on (111) surface; thus, the surface spectrum can only be characterized as $\sqrt{{v_x}^2{k_x}^2 + {v_y}^2{k_y}^2}$ with $v_x = v_y$ at $\bar{\Gamma}$ and $v_x \neq v_y$ at $\overline{M}$ to obey all the symmetry constrains. This type-I Dirac surface manifests as a circular Fermi surface on the energy contour similar to the bismuth chalcogenide Z_2 topological insulators [35].

An important property of the type-II Fermi surface is the contact of open electron and hole pockets. According to Fig. 4(d), when the Fermi level is varied from -0.13 eV to -0.08 eV, the energy contour on the (110) surface reveals that the Fermi surfaces with electron and hole characters approach closer to and intersect each other at the type-II Dirac point with the energy of -0.126 eV. This energy level coincides with the linear band crossing in the $\overline{\Gamma X}$ direction in the (110) surface energy band structure. In addition, since there are two Dirac points on the opposite side of $\overline{X}(0.5,0)$, there is also a Lifshitz transition on the Fermi surface. However, different from the type-I Dirac surface, the connecting and disconnecting of the holelike and electronlike pockets do not exhibit a crescent shape. Specifically, when the energy level is varied from -0.08 to -0.126 eV, the enlarged hole Fermi surface first separates from each other to form conical shape, increasing in size as the Fermi level is lowered to the bulk valence band. These conical shapes exhibit a single point connection at -0.126 eV, representing the type-II Dirac point. As the energy level is further reduced, the point touching of the Fermi surface disappears, and the topological surface state is now merged into the bulk bands. The different behaviors of the type-I and the type-II Dirac surfaces can be used as an experimental signature to detect these new types of topological surface states.

C. Type-I and type-II Dirac surface in Ca_2HgPb

Since the band inversion also occurs in Ca_2HgPb, it is expected that the topological surfaces also occur in this material. As shown in Fig. 5, the energy spectra of the [001] and [110]-orientations reveal a pair of type-II Dirac points along the $\overline{\Gamma X_1}$ and $\overline{\Gamma X}$ in the 2D Brillouin zone. Moreover, a type-I Dirac point is also observed at $\bar{\Gamma}$ on the (001) surface and along the $\overline{\Gamma X}$ line on the (110) surface. The type-I Dirac node on the (110) surface can be characterized as an accidental crossing between the topological surface state and the Rashba splitting of the normal surface band. On the other hand, on the [001] orientation, in addition to the (110) mirror plane, there is an additional reflection from the (001) plane mapping $x \rightarrow -x$ direction also perpendicular to the (001) surface, which can potentially induce a nonzero mirror number. To validate this

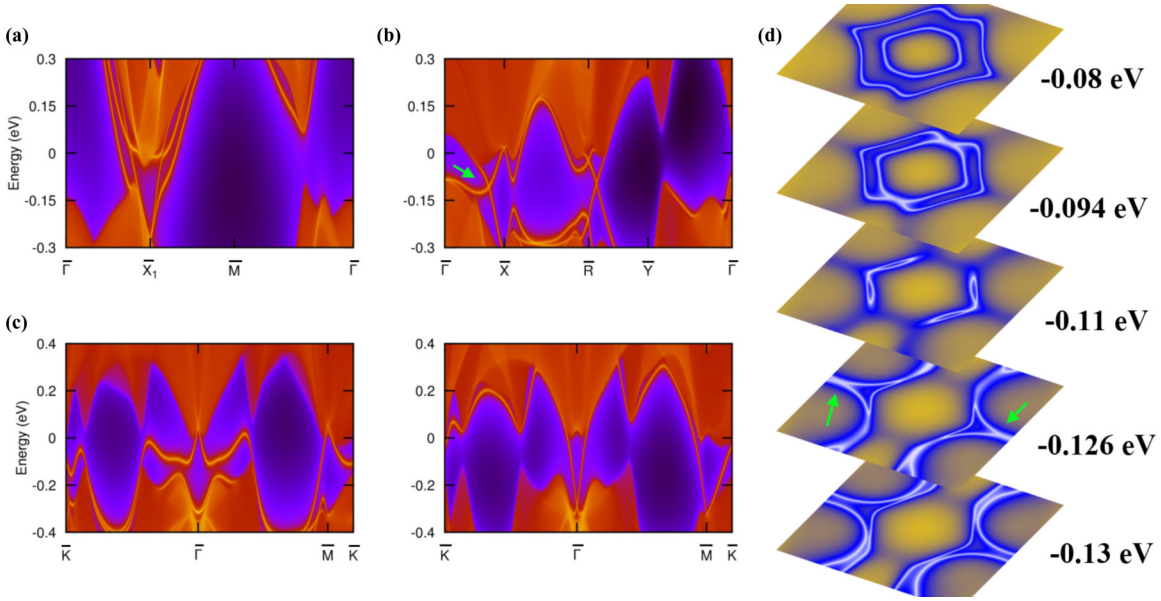

FIG. 4. Surface energy spectrum and Fermi surfaces of type-II TCI Li_2BiTl. (a) [001] orientation with Tl-Bi termination; (b) [110] orientation; (c) [111] orientation with Tl (left) and Bi (right) termination. (d) Constant energy contours of the [110] orientation at different levels. The green arrow shows the type-II Dirac node. The energy spectra were obtained from 50 slabs.

conception, the Wilson loop method [36–38] was employed to determine the MCN on the $x = 0$ plane. As shown in the Supplementary Material [34], the Wannier charge centers on the $x = 0$ plane obtained from the i and $-i$ eigenbasis of the reflection mirror operator reveal a nontrivial Chern number. Thus, the topology in Ca_2HgPb is protected by not only the (110) plane but also by the (001) plane. Since there is one type-I Dirac point at $\bar{\Gamma}$ and two type-II Dirac points along $\overline{\Gamma X_1}$, it can be inferred that the [001] surface of Ca_2HgPb has two different MCNs of $|N_m| = 2$ and 1 associated with two different mirror planes. The Wilson loop calculations were also performed for other Hg-based FH materials for the same $x = 0$ plane. The results show that Ca_2HgSn and Sr_2HgPb also contain a MCN of 1, while the MCN associated with the $x = 0$ plane for Ba_2HgPb is 0. On the [111] orientation, Ca_2HgPb exhibits only the type-I Dirac surfaces, similar to Li_2BiTl and Ca_2AuBi.

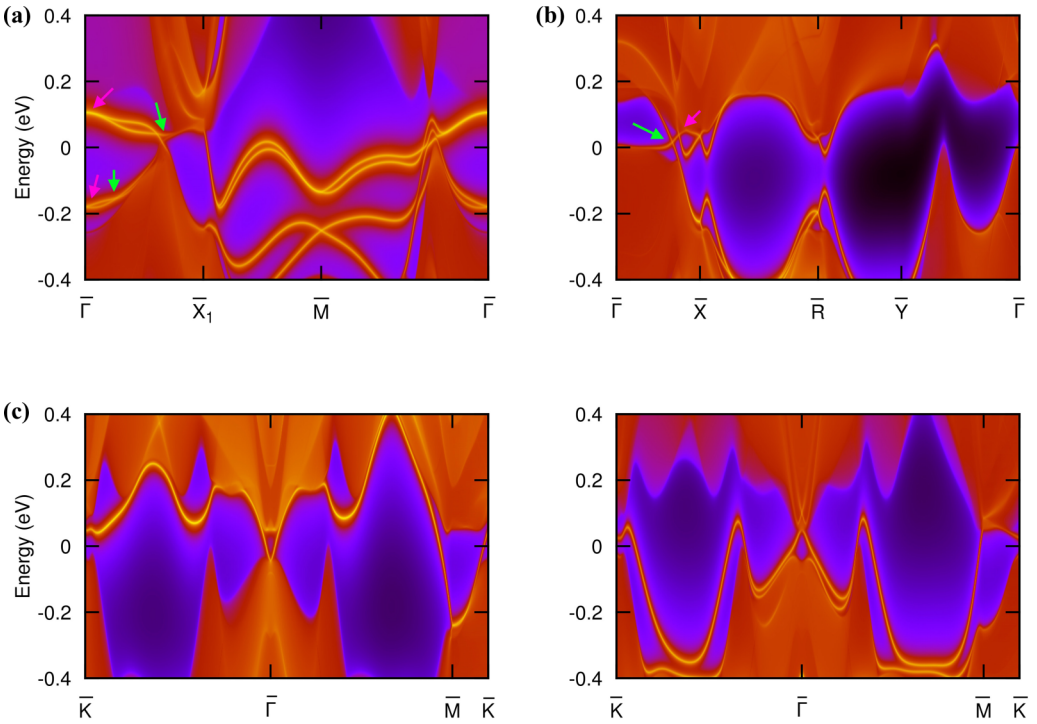

FIG. 5. Surface energy spectrum of type-II Dirac fermions in Ca_2HgPb. (a) The [001] orientation with Hg-Pb termination; (b) [110] orientation; (c) [111] orientation with Hg (left) and Pb (right) termination. The green arrow highlights the type-II Dirac point

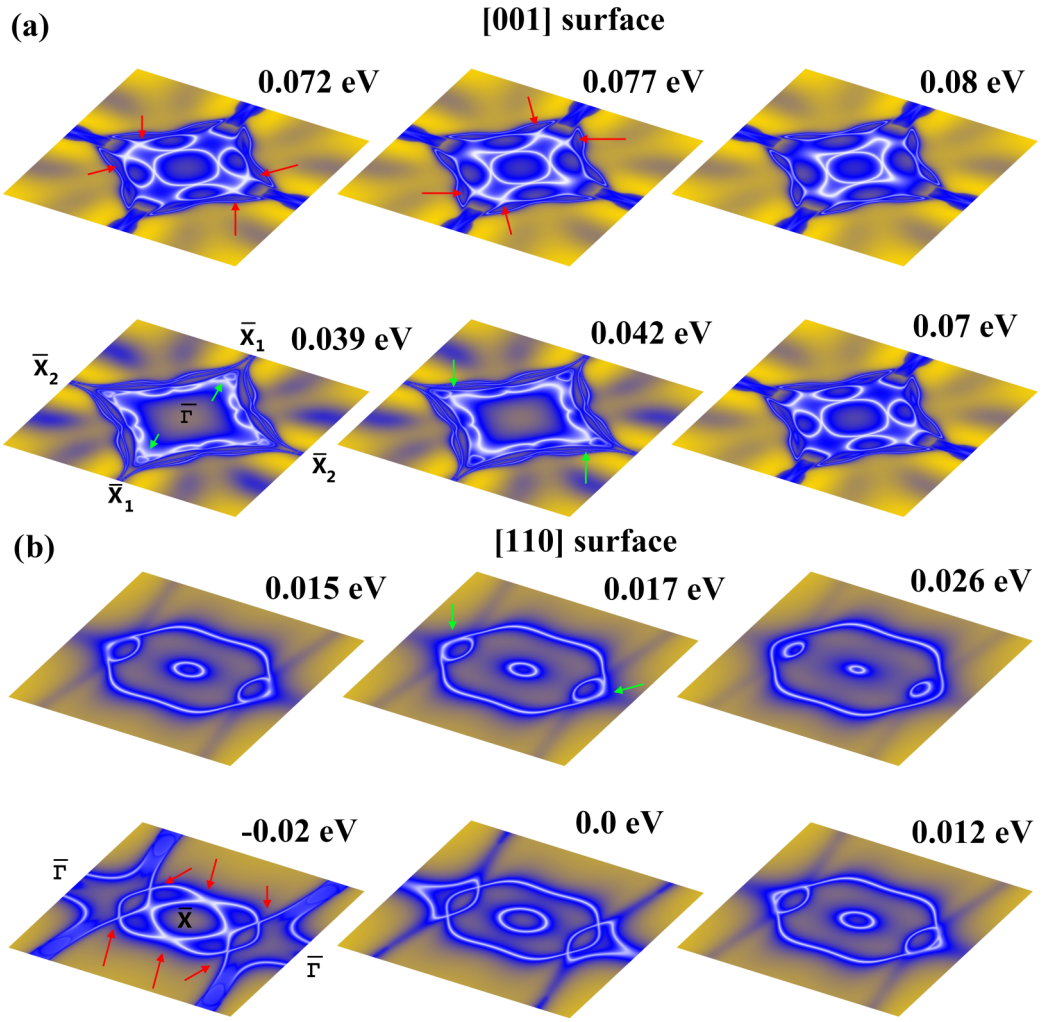

FIG. 6. Constant energy contours of Ca_2HgPb on the [001] and [110] orientation. The red arrows show the Lifshitz transitions, and the green arrows show the type-II Dirac cones corresponding to Fig. 5.

To further understand the topological properties of these different Dirac points, the Fermi surfaces were investigated on the (001) and (110) surfaces. As shown in Fig. 6, the constant energy contours reveal multiple Lifshitz transitions on the (001) and (110) surfaces. In the [001] orientation, the two type-II Dirac nodes situated away from $\overline{X_1}(\overline{X_2})$ points, which undergo two Lifshitz transition and merge together at $\bar{\Gamma}$. In addition, the type-I Dirac point is also manifested itself as an enclosed circular surface. For the energy contours on the (110) surface, the multiple Lifshitz transition occur inside the bulk valence band and form a connected elliptical contour with a circular shape centered at $\overline{X}$. The type-II Dirac nodes are formed at 0.017 eV due to the touching of the circular hole pocket and the electron pocket. This hole pocket is then shrunk in size and becomes a circular type-I Dirac node with increasing Fermi level due to the accidental band crossing of the topological surface state and the Rashba surface state. Hence, the behaviors of the topological surface states and the corresponding Fermi surfaces show a rich interplay between the bulk material chemistry and the mirror planes, which can give rise to multiple protected topological surfaces with different characteristics in the same material. Furthermore, the Hg-based FH material can be considered as an example of a layer-coupled TCI [39] due to the quasi-2D nature of the FH structure. The breaking of different mirror symmetry through nanostructuring can create interesting effects such as room-temperature ferroelectricity [40], as well as a potential application in magnetically controlled nanodevice due to the anomalous magnetic behavior in type-II Dirac surfaces [41], which cannot be achieved in other material systems.

VI. CONCLUSIONS

In conclusion, we have reported the existence of exotic topological surfaces in a new family of TCI materials with FH structure, which can host different Dirac quasiparticles. We revealed the experimental signatures of the type-II Dirac surface as the touching of the electron and hole pockets on the Fermi surfaces. In addition, the role of the different mirror planes in the layered FH is also explored, showing a new type of TCI with multiple protected mirror planes. Thus, our paper also opens up a pathway to exploit the topological properties of TCI for fundamental and practical applications

due to the versatility of the FH materials. By substituting the appropriate elements in the three sites, the interplay of mirror symmetry can be manipulated to realize the magnetism, superconductivity, thermoelectricity, and topological surface transitions.

ACKNOWLEDGMENTS

We acknowledge the support of the Australian Research Council via the Discovery Grants No. DP150103006 and No. DP140104373. The computational resources were supported by the National Computing Infrastructure.

[1] L. Fu, Phys. Rev. Lett. **106**, 106802 (2011).
[2] Y. Ando and L. Fu, Annu. Rev. Condens. Matter Phys. **6**, 361 (2015).
[3] T. H. Hsieh, H. Lin, J. Liu, W. Duan, A. Bansil, and L. Fu, Nat. Commun. **3**, 982 (2012).
[4] J. Liu, W. Duan, and L. Fu, Phys. Rev. B **88**, 241303(R) (2013).
[5] Y. J. Wang, W. F. Tsai, H. Lin, S. Y. Xu, M. Neupane, M. Z. Hasan, and A. Bansil, Phys. Rev. B **87**, 235317 (2013).
[6] S. Safaei, P. Kacman, and R. Buczko, Phys. Rev. B **88**, 045305 (2013).
[7] Y. Tanaka, Z. Ren, T. Sato, K. Nakayama, S. Souma, T. Takahashi, K. Segawa, and Y. Ando, Nat. Phys. **8**, 800 (2012).
[8] P. Dziawa, B. J. Kowalski, K. Dybko, R. Buczko, A. Szczerbakow, M. Szot, E. Łusakowska, T. Balasubramanian, B. M. Wojek, M. H. Berntsen, O. Tjernberg, and T. Story, Nat. Mater. **11**, 1023 (2012).
[9] S.-Y. Xu, C. Liu, N. Alidoust, M. Neupane, D. Qian, I. Belopolski, J. D. Denlinger, Y. J. Wang, H. Lin, L. A. Wray, G. Landolt, B. Slomski, J. H. Dil, A. Marcinkova, E. Morosan, Q. Gibson, R. Sankar, F. C. Chou, R. J. Cava, A. Bansil *et al.*, Nat. Commun. **3**, 1192 (2012).
[10] Y. Okada, M. Serbyn, H. Lin, D. Walkup, W. Zhou, C. Dhital, M. Neupane, S. Xu, Y. J. Wang, R. Sankar, F. Chou, A. Bansil, M. Z. Hasan, S. D. Wilson, L. Fu, and V. Madhavan, Science **341**, 1496 (2013).
[11] A. A. Soluyanov, D. Gresch, Z. Wang, Q. Wu, M. Troyer, X. Dai, and B. A. Bernevig, Nature (London) **527**, 495 (2015).
[12] T. R. Chang, S. Y. Xu, G. Chang, C. C. Lee, S. M. Huang, B. Wang, G. Bian, H. Zheng, D. S. Sanchez, I. Belopolski, N. Alidoust, M. Neupane, A. Bansil, H. T. Jeng, H. Lin, and M. Z. Hasan, Nat. Commun. **7**, 10639 (2016).
[13] K. Koepernik, D. Kasinathan, D. V. Efremov, S. Khim, S. Borisenko, B. Büchner, and J. van den Brink, Phys. Rev. B **93**, 201101(R) (2016).
[14] Z. Wang, D. Gresch, A. A. Soluyanov, W. Xie, S. Kushwaha, X. Dai, M. Troyer, R. J. Cava, and B. A. Bernevig, Phys. Rev. Lett. **117**, 056805 (2016).
[15] S. Y. Lin, M. Chen, X. B. Yang, Y. J. Zhao, S. C. Wu, C. Felser, and B. Yan, Phys. Rev. B **91**, 094107 (2015).
[16] S. Chadov, X. Qi, J. Kübler, G. H. Fecher, C. Felser, and S. C. Zhang, Nat. Mater. **9**, 541 (2010).
[17] H. Lin, L. A. Wray, Y. Xia, S. Xu, S. Jia, R. J. Cava, A. Bansil, and M. Z. Hasan, Nat. Mater. **9**, 546 (2010).
[18] Z. Wang, M. G. Vergniory, S. Kushwaha, M. Hirschberger, E. V. Chulkov, A. Ernst, N. P. Ong, R. J. Cava, and B. A. Bernevig, Phys. Rev. Lett. **117**, 236401 (2016).
[19] L. Fu and C. L. Kane, Phys. Rev. B **76**, 045302 (2007).
[20] I. Galanakis, P. H. Dederichs, and N. Papanikolaou, Phys. Rev. B **66**, 174429 (2002).
[21] J. He, M. Amsler, Y. Xia, S. S. Naghavi, V. I. Hegde, S. Hao, S. Goedecker, V. Ozoliņš, and Chris Wolverton, Phys. Rev. Lett. **117**, 046602 (2016).
[22] P. E. Blochl, Phys. Rev. B **50**, 17953 (1994).
[23] G. Kresse and D. Joubert, Phys. Rev. B **59**, 1758 (1999).
[24] H. J. Monkhorst and J. D. Pack, Phys. Rev. B **13**, 5188 (1976).
[25] J. P. Perdew, K. Burke, and M. Ernzerhof, Phys. Rev. Lett. **77**, 3865 (1996).
[26] J. Heyd, G. E. Scuseria, and M. Ernzerhof, J. Chem. Phys. **118**, 8207 (2003).
[27] J. Heyd and G. E. Scuseria, J. Chem. Phys. **121**, 1187 (2004).
[28] J. Vidal, X. Zhang, L. Yu, J.-W. Luo, and A. Zunger, Phys. Rev. B **84**, 041109(R) (2011).
[29] N. Marzari and D. Vanderbilt, Phys. Rev. B **56**, 12847 (1997).
[30] I. Souza, N. Marzari, and D. Vanderbilt, Phys. Rev. B **65**, 035109 (2001).
[31] M. P. Sancho, L. Sancho, J. M. L. Sancho, J. M. L. Sancho, and J. Rubio, J. Phys. F Met. Phys. **15**, 851 (1985).
[32] Q. S. Wu and S. N. Zhang, Wannier_tools. https://github.com/quanshengwu/ wannier_tools.
[33] A. Togo and I. Tanaka, Scr. Mater. **108**, 1 (2015).
[34] See Supplemental Material at http://link.aps.org/supplemental/10.1103/PhysRevB.95.115124 for the bulk band structures, the surface spectrum, the Wannier charge center calculation, and the phonon spectrum.
[35] Y. L. Chen, J. G. Analytis, J. H. Chu, Z. K. Liu, S. K. Mo, X. L. Qi, H. J. Zhang, D. H. Lu, X. Dai, Z. Fang, S. C. Zhang, I. R. Fisher, Z. Hussain, and Z. X. Shen, Science **325**, 178 (2009).
[36] R. Yu, X. L. Qi, A. Bernevig, Z. Fang, and X. Dai, Phys. Rev. B **84**, 075119 (2011).
[37] H. Weng, X. Dai, and Z. Fang, MRS Bull. **39**, 849 (2014).
[38] H. Weng, C. Fang, Z. Fang, B. A. Bernevig, and X. Dai, Phys. Rev. X **5**, 011029 (2015).
[39] I. C. Fulga, N. Avraham, H. Beidenkopf, and A. Stern, Phys. Rev. B **94**, 125405 (2016).
[40] K. Chang, J. Liu, H. Lin, N. Wang, K. Zhao, A. Zhang, F. Jin, Y. Zhong, X. Hu, W. Duan, Q. Zhang, L. Fu, Q.-K. Xue, X. Chen, and S.-H. Ji, Science **353**, 274 (2016).
[41] C.-K. Chiu, Y.-H. Chan, X. Li, Y. Nohara, and A. P. Schnyder, Phys. Rev. B **95**, 035151 (2017).